

Simulation of the spray drying of single granules: The correlation between microscopic forces and granule morphology

Thomas Breinlinger^a, Adham Hashibon^a, Torsten Kraft^a,

^aFraunhofer Institute for Mechanics of Materials IWM, 79108 Freiburg, Germany

Abstract

In the ceramic industry, spray drying is an important process transforming fine primary powder into processable granular material. Granule formation at spray drying has been investigated in the past and plausible explanatory models have been established for the governing mechanisms of granule formation. In this study we use numerical modeling via coupled discrete element method (DEM) and computational fluid dynamics (CFD) simulations to investigate this formation process. The focus lies on the evolution of the granule morphology during drying of single droplets. Besides demonstrating that the simulation results support the propositions made by the experimentally-based models a new correlation was found which leads to an extension of those models for granule formation in terms of the granule stability.

Keywords: Spray drying, granulation, morphology, surface tension, capillary force, DEM, CFD

1. Introduction

Spray drying is an important process in powder technology, e.g. in the ceramic industry. It is used to transform raw material, which is available in the form of very fine primary powder, to coarser granules because fine powders are highly adhesive and, hence, do not flow well [1]. In the process chain of dry pressing and sintering, it is important to have granules with low porosity to allow for good quality of the final product. The reason for this is that hollow and porous granules often feature bad compressibility leading to voids which could create defects in the sintered product [2].

The spray drying process uses a ceramic suspension, which is a mixture of a liquid carrier phase and the solid ceramic particles suspended within. Depending on different parameters such as the *pH* as well as binder and dispersant content, the solid particles are either well dispersed or agglomerated – the suspension is therefore referred to as stable or unstable, respectively [3]. Numerous experimental investigations showed that the stability of the suspension has a major influence on the final granule morphology, i.e. well dispersed suspensions often lead to hollow granules [4–9]. Hence, the interparticle forces, which are responsible for the state of the suspension (e.g. dispersed vs. agglomerated), play an important role in the evolution of the granule morphology. On the other hand, there is also the capillary force exerted on the primary particles

Email address: thomas.breinlinger@iwm.fraunhofer.de (Thomas Breinlinger)

by the receding liquid surface that creates a compressive drying stress inside the particle network during drying [3]. However, the effects of this force have not been studied experimentally in the context of spray drying of ceramics, which might be caused by difficulty of varying the surface tension without changing other important suspension parameters.

Besides experimental research, simulation studies have also been carried out to investigate granule formation during spray drying processes. Basic approaches use one dimensional models of heat and mass transfer [10, 11] to describe the drying of rotationally symmetric drops depending on the suspension parameters and process conditions. By taking into account transport through porous media, shell formation can also be modeled to some extent [12]. These approaches can be used as sub-models for process scale simulations for the tracking of drying granules through the drying chamber. Another class of models use a stochastic description of the suspended particles based on a population balance [13]. This approach allows e.g. distinguishing between wet and dry shell and enables the simulation of shell growth [14] and even provides some insight regarding the granule morphology [15], albeit still on an averaged level, i.e. without specific details of the microscopic structure and variations of the particle distribution. In summary, none of the above approaches can provide detailed information about the evolution of the granule morphology on the level of solid particles.

Contrary to the above approaches, the discrete element method (DEM) can provide this level of detail as it describes the solid phase as many individual particles. E.g., by using the DEM, Greil et al. [16] simulated the electrophoretic deposition of particles on a substrate. Recently, the first (and to our best knowledge the only) drop scale simulations of spray drying, using the DEM, have been published [17, 18]. By coupling the DEM with computational fluid dynamics (CFD), these simulations are able to resolve the granule formation on solid particle level and, hence, provide information about the evolution of the granule morphology. The simulations reported so far showed a trend to hollow granules at high temperatures [17] and binder content [18]. However, none of these studies has included an investigation of the effects of the basic interparticle forces or of the capillary surface tension on the evolution of the granule morphology and their final form.

In this work, we investigate the role of interparticle forces on the evolution of the granule morphology using coupled CFD-DEM simulations. For a number of reasons discussed later on, we use a coarsened approach where *one DEM particle* always represents *a number of primary particles* – either agglomerated or dispersed. Therefore, it is crucial to always be aware that the DEM forces in this work do *not* model directly the real interparticle forces but are derived from the behavior of many primary particles interacting with each other. Hence, they are describing the granular phase in a coarsened, effective way.

The goal of this study is to test the established models of granule formation, which are mostly based on particle mobility [4, 6, 7] and, in addition, to further investigate specifically the role of the bulk cohesive and capillary forces during the formation of the particle network. A comparison of the influence of the forces of different nature is engaged to identify correlations and to extend the models for granule formation.

2. Methods

The solver we used in this study is a coupled CFD-DEM program that includes evaporation of the liquid carrier phase. It is implemented in OpenFOAM® version 2.2.1 [19], as a customized combination of the standard solvers *interFoam* and *icoUncoupledKinematicParcelFoam*. The following sections briefly describe the underlying models.

2.1. Multiphase fluid dynamics with evaporation

Using the volume of fluid method (VoF) for multiphase flow [20] and the locally averaged coupling with a discrete phase [21], the motion of two incompressible fluid phases, e.g. water and air, carrying solid particles is governed by the averaged Navier-Stokes equations

$$\nabla \mathbf{v} = 0 \quad (1)$$

$$\rho \frac{\partial \mathbf{v}}{\partial t} = -\nabla p + \mu \nabla^2 \mathbf{v} + \sigma \kappa \frac{\nabla \alpha}{|\nabla \alpha|} + \rho \mathbf{g} + \mathbf{f}_c, \quad (2)$$

where \mathbf{v} is the velocity, p is the pressure and \mathbf{g} is the gravity. Surface tension is included by the term $\sigma \kappa \nabla \alpha / |\nabla \alpha|$, where σ is the surface tension coefficient and κ is the curvature of the liquid surface. The term \mathbf{f}_c represents volumetric coupling forces from the solid particles within a computational cell and will be discussed later. The average density ρ and viscosity μ in each cell are computed based on the phase function α , which determines the ratio of water in each cell, as

$$\rho = \rho_l \alpha + \rho_g (1 - \alpha), \quad \mu = \mu_l \alpha + \mu_g (1 - \alpha), \quad (3)$$

Here the indices l and g represent the liquid and gas phase, respectively. The term $\sigma \kappa (\nabla \alpha) / |\nabla \alpha|$ represents the surface tension force, where σ and κ are the surface tension parameter and surface curvature, respectively. The phase function is balanced by its own transport equation

$$\frac{\partial \alpha}{\partial t} + \nabla \cdot \mathbf{v} \alpha = \dot{\alpha}_{ev}, \quad (4)$$

where the $\dot{\alpha}_{ev}$ is a source term which extends the established VoF scheme to incorporate evaporation during the drying process. To model this, we use the source term

$$\dot{\alpha}_{ev} = -\frac{1}{2} D \kappa \frac{(c_f - c_\infty)}{\rho} |\nabla \alpha|, \quad (5)$$

which describes isothermal diffusion controlled phase change. Here D is the diffusion coefficient and c_f and c_∞ are the vapor concentrations in the evaporation film and at ambient conditions, respectively. For the sake of boundedness of the phase function and stability of the solution, the application of $\dot{\alpha}_{ev}$ was limited to regions where $0 \leq \alpha \leq 1$.

2.2. Discrete phase

In this work we use the Discrete Element Method (DEM) [22] to describe the granular media. This method describes the motion of a particle by integrating Newton's equations of motion

$$m_i \dot{\mathbf{v}}_i = \mathbf{F}_i^{tot}, \quad (6)$$

where m_i and \mathbf{v}_i denote the mass and velocity of DEM particle i , respectively and \mathbf{F}_i^{tot} is the total force on DEM particle i which is calculated as the sum of all the interaction and coupling forces introduced in the following.

Brief reviews of DEM contact forces are available e.g. from [23] and [24]. The contact model used in this work consists of elastic repulsion, dissipation, cohesion and friction. These forces are applied whenever two DEM particles have a positive overlap $h_{ij} = |\mathbf{x}_i - \mathbf{x}_j| - (r_i + r_j)$, where \mathbf{x} and r are the DEM particle position and radius, respectively. The elastic repulsion is described following [25] as

$$\mathbf{F}_{ij}^e = \left(\frac{2}{3} \bar{E} \sqrt{\bar{r}_{ij}} h_{ij}^{3/2} \right) \hat{\mathbf{x}}_{ij}, \quad (7)$$

in normal direction $\hat{\mathbf{x}}_{ij} = (\mathbf{x}_i - \mathbf{x}_j)/|\mathbf{x}_i - \mathbf{x}_j|$. Here \bar{r}_{ij} represents the effective DEM particle radius $\bar{r}_{ij} = r_i r_j / (r_i + r_j)$ and $\bar{E} = E / (1 - \nu^2)$ is the effective Young's modulus with the Poisson number ν . The viscous part of the collision, which represents dissipation by plastic deformation, is modeled as a velocity dependent damping force [26]

$$\mathbf{F}_{ij}^v = - \left(\gamma \sqrt{\bar{r}_{ij} h_{ij}} \mathbf{v}_{ij} \cdot \hat{\mathbf{x}}_{ij} \right) \hat{\mathbf{x}}_{ij}. \quad (8)$$

The damping parameter γ is determined empirically. Cohesion between the DEM particles is modeled based on the overlap area A of the contact

$$\mathbf{F}_{ij}^c = - (\omega_A A) \hat{\mathbf{x}}_{ij}, \quad (9)$$

where ω_A is the cohesive force per unit area or work of separation per unit volume. Friction between the DEM particles is modeled as a tangential force [22]

$$\mathbf{F}_{ij}^f = - \min \left[\kappa \sqrt{\frac{h_{ij}}{\bar{r}_{ij}}} |\xi_{ij}|, \mu |\mathbf{F}_{ij}^e + \mathbf{F}_{ij}^v| \right] \frac{\xi_{ij}}{|\xi_{ij}|} \quad (10)$$

based on the relative displacement ξ_{ij} of the initial contact points its magnitude is governed by the tangential spring constant κ and the friction parameter μ .

2.3. Coupling forces

Coupling between CFD and DEM was established based on cell level averaging [21], i.e. the volumetric coupling force \mathbf{f}_c in the momentum equation (2) was calculated for each cell as the sum of the total coupling force \mathbf{F}^{coup} of all DEM particles inside the cell (figure 1, a)

$$\mathbf{f}_c = \mathbf{F}^{coup} / V_{cell}. \quad (11)$$

Here V_{cell} is the volume of the computational cell. The coupling forces used in this work are introduced in the following.

For a DEM particle inside a fluid, the drag force can be estimated by Stoke's law

$$\mathbf{F}_i^s = 6\pi\mu r_i \mathbf{v}_i. \quad (12)$$

In cases where a relative velocity between the fluid and the particles exists, the drag force must be included in the coupling. In the present case, however, there is no significant physical current inside the fluid. In contrast, due to the VoF model, there are intrinsic artificial currents [27–29] that can induce a significant error on the particle formation. Therefore, the drag force was turned off during the presented simulations.

If a DEM particle is at the liquid surface, two forces occur: a pressure force arising from the pressure jump across the liquid surface and a capillary force exerted on the DEM particles by the surface tension acting on the contact line. The pressure force is [30]

$$\mathbf{F}^{\Delta p} = A_w \Delta p \hat{\mathbf{n}}, \quad (13)$$

where A_w is the cross sectional area at the intersection plane, which is a circle with wetting radius r_w , $\hat{\mathbf{n}}$ is the surface normal and Δp is the pressure jump across the surface, which follows from the Young-Laplace equation $\Delta p = 2\sigma\kappa$, where again κ is the surface curvature and σ is the surface

tension. However, in this paper the pressure force is not taken into account because it contradicts to the cell averaged resolution of the coupling [30].

In order to determine the capillary force for arbitrary regimes, one has to know the size and curvature of the capillary necks (or bridges) at the DEM particle-surface contacts [31]. However, if the necks are sufficiently small, they can be neglected and the capillary force can be estimated from an integral of the surface tension over the contact line [32]. Doing so, the capillary force becomes (see figure 1, b)

$$\mathbf{F}^{cap} = 2\pi r\sigma \sin(\omega) \sin(\omega + \Theta) \hat{\mathbf{n}}, \quad (14)$$

where Θ is the contact angle [30]. The angular position of the contact line ω is defined in figure 1 (b) and can be calculated as $\omega = \arccos(-h_c/r)$, where h_c is the distance of the DEM particle center from the liquid surface. This distance is defined by $h_c = (\alpha_b - \alpha_p) / |\nabla\alpha_p|$, where α_p is the scalar value at the DEM particle and α_b represents the phase boundary. In the context of volume of fluid, where $0 \leq \alpha \leq 1$, this boundary is at $\alpha_b = 0.5$.

2.4. Modeling of drying suspensions

The ceramic suspensions used in spray drying are usually aqueous solutions of primary particles (often alumina or zirconia) with sizes of the order of sub-micron to a few micrometers and a typical solid content somewhere around 30 – 40 vol.% [4, 6, 7, 9, 33]. The spray dried granules often exceed 100 μm yielding a granule-particle size ratio of 100 or more and leading to a large number of primary particles ($10^5 - 10^6$) in a single granule. As the primary particles are so small, their physical interparticle forces are repulsive as well as attractive and can be described by the DLVO theory [34].

During the drying of the initial drops, the ceramic suspension may undergo a drastic change, especially at the liquid surface. In this region, many parameters change during drying, e.g. the solid content, the binder concentration and the dispersant concentration. In addition, once the liquid surface penetrates the newly forming primary particle network, liquid bridges may form and evaporate adding an additional mode of time dependent cohesion. All of the above effects are not straight forward to quantify.

Additionally, in the simulations the number of DEM particles that can be used is limited by computational resources. Therefore, it is a common practice in DEM simulations to revert to coarse graining [35], where a number of real particles are clustered and modeled by one larger, DEM particle, which still directly imitates the primary particle behavior. In our case, transferring the original models (i.e. DLVO etc.) to the coarse grained DEM scale would require several steps which include (i) the parametrization of the original models, (ii) transforming them to the

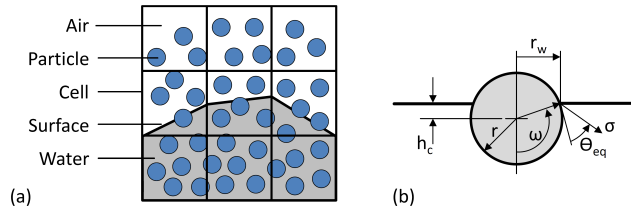


Figure 1: (a): Schematic illustration of CFD-DEM simulations using local averaging. (b): DEM particle-surface contact with negligible local curvature as assumed by the model.

coarsened level, (iii) fit the original models into DEM context and (iv) scale the parameters to get reasonable DEM time steps. This transformation is particularly challenging, as the real primary particles experience microscopic features such as a repulsive barrier, which acts on a certain length scale.

In order to limit the mentioned complexity and to reduce the number of parameters, we introduced a coarsening technique similar to the classic coarse graining, which we refer to as the effective particle model. In this model a single DEM particle represents a lump of primary particles describing their bulk behavior in different states of the suspension in an effective way. The most important feature of this technique is that the effective cohesion ω between the DEM particles is *not* immediately related to the cohesive part of the primary particle potential but is used to effectively model the *bulk strength* of an evolving primary particle network. The precise reason for this is discussed in more detail in section 4.1. Figure 2 briefly illustrates this model for agglomerated (a) and dispersed (b) suspensions. The resulting model uses only two parameters to characterize the state of the suspension: an effective wet cohesion ω_i which acts inside the liquid region and an effective dry cohesion ω_o which acts on the outside. These two parameters can be set individually, but in this study the effective wet cohesion ω_i was always chosen to be smaller than or equal to the effective dry cohesion ω_o . In the region close to the liquid surface, the effective cohesion for each DEM particle contact was calculated by blending both linearly as

$$\omega_{eff} = c_\omega \omega_o + (1 - c_\omega) \omega_i, \quad (15)$$

to prevent discontinuities. The blending parameter c_ω is defined as

$$c_\omega = \begin{cases} 0 & \text{for } \alpha_{ij} \leq 0 \\ 2\alpha_{ij} & \text{for } 0 \leq \alpha_{ij} \leq 0.5 \\ 1 & \text{for } 1 \leq \alpha_{ij} \end{cases} \quad (16)$$

with the contact mean phase fraction $\alpha_{ij} = (\alpha_i + \alpha_j)/2$.

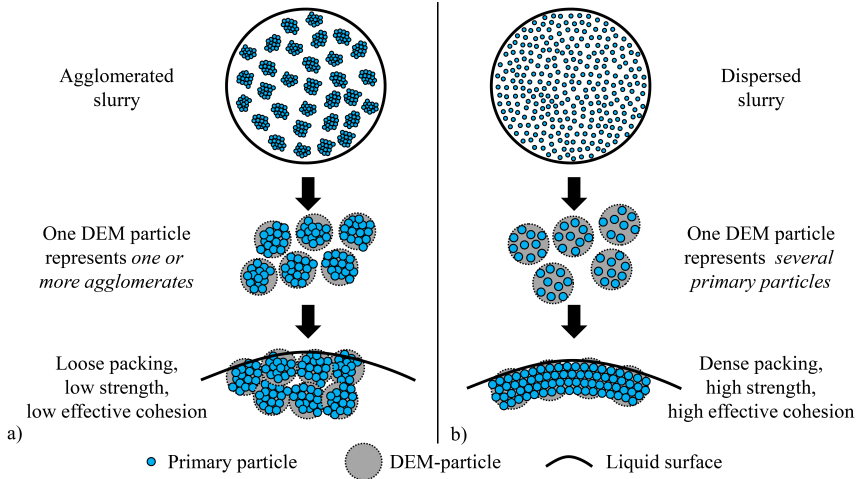


Figure 2: Schematic illustration of the coarsened effective DEM particle model of agglomerated (a) and dispersed suspensions (b).

As described above, these effective cohesion parameters do not reflect the primary particle potential but act to effectively imitate the structural and mechanical properties of the evolving primary particle network, i.e. the granule shell. Thus, the state of the suspension (i.e. dispersed vs. agglomerated) is represented by the effective cohesion parameters in a counter intuitive way: Dispersed slurries form dense and stable networks and are, therefore, reflected by a large effective cohesion parameter, while agglomerated slurries form coarser networks of reduced strength, which corresponds to a lower effective cohesion parameter.

2.5. Case setup

We applied the model described above to the simulation of individual drying droplets of ceramic suspensions. The setup of the 3D simulations consisted of a cubic box of 1 mm edge length discretized with 30 cells per direction. At the center of this box, a drop of 500 μm diameter was placed and filled with DEM particles of diameter 20 μm . Figure 3 shows the initial setup, displaying the computational cells (left) and domain (right) along with the DEM particles (colored randomly) and the liquid surface (green).

Water was chosen for the carrier fluid, as it is commonly used in the spray drying of ceramics [3, 9]. The filling ratio of 30 vol% also agrees with practical applications [4, 6]. The air temperature was chosen to be 150 °C, which approximately corresponds to the average of temperatures found in literature for Al_2O_3 (100 – 200 °C) [4, 9]. The precise wetting angle of water on the primary particles is hard to determine, hence, we chose a value of 60°, which contributes to the stability of the suspension [30]. As discussed in section 2.4, many primary particles, which are often of the order of 1 μm or even smaller, were grouped together to form an effective DEM particle of 20 μm . As these effective particles resemble a lump of primary particles and, thus, are not fully dense, we reduced the particle density from 3.94 g/mm^3 (Al_2O_3) to 2 g/mm^3 . The friction coefficient was set to a the relatively high value of 2 in order to accommodate geometric jamming, which might happen on the primary particle level. Finally, the effective cohesion parameters ω_i and ω_o are based on a strongly simplified model and, therefore, have been parametrized with generic values. These parameters could in principle be derived from simulations on primary particle scale by simulating drying of a small volume of suspension followed by a simulation of the mechanical strength of the dried specimen. In this study, a reasonable parameter space has been determined in preliminary test runs instead. The simulation parameters are summarized in table 1.

2.6. Post-processing

For the dried granules we analyzed the overall granule density as the sum of all DEM particle volumes divided by the total volume of a convex hull encompassing the granule. This hull was calculated using a Delaunay triangulation of the particles center points, shifted outwards by half their radius. In addition, we analyzed the granule morphology by calculating the local pore size all over the granule using a Voronoi tessellation of the original particle center points. The local porosity was evaluated as Voronoi volume divided by particle volume. Plotting the local porosity over the granule radius creates a diagram where dense and porous regions can be clearly identified, allowing for measurement of the size of the different regions (e.g. shell thickness). Both Delaunay and Voronoi analysis were carried out using the SciPy Python package [36].

Parameter	Unit	Section 3.1	Section 3.2
Drop diameter	μm	500	500
Solid content	<i>vol%</i>	30	30
Fluid density	g/cm^3	1	1
Fluid viscosity	m^2/s	10^{-4}	10^{-4}
Diffusion coefficient	mm^2/s	20.7	20.7
Temperature	$^{\circ}C$	150	150
Particle density	g/cm^3	2	2
Wetting angle	$^{\circ}$	60	60
Effective cohesion dry	kN/m^2	50...350	150
Effective cohesion wet	kN/m^2	0...350	0...150
Surface tension	mN/m	7.07	0.707...70.7
Particle diameter	μm	20	20
Friction coefficient	–	2	2

Table 1: Model parameters for the simulation of spray drying.

3. Results

3.1. Cohesion

In the first part of this section, we investigated the influence of the cohesion parameters on the drying of the granules. For this purpose, we varied both dry and effective wet cohesion within the range of $\omega_o = 50 \dots 350 \text{ kN/m}^2$ and $\omega_i = 0 \dots 350 \text{ kN/m}^2$, respectively, with ratios of $\omega_i/\omega_o = 0, 0.1, 0.5$ and 1. For the case of $\omega_o = 150 \text{ kN/m}^2$, figure 4 shows cross sectional slices through the three granules with $\omega_i/\omega_o = 0, 0.5$ and 1. The slices shown here have a thickness of roughly two DEM particles. We observe a dense granule for low effective cohesion ratio ω_i/ω_o (i.e. low wet cohesion) and hollow granules for higher ratios.

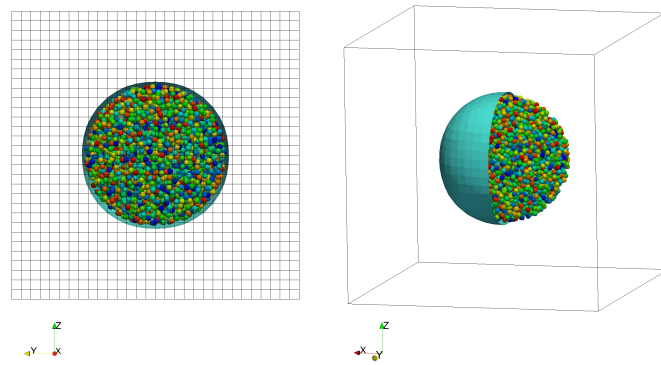


Figure 3: Initial constellation of a simulation with a solid content of 30 *vol.%*. Left: Computational grid and drop in *yz*-plane. Right: Computational domain with drop surface (green, half plot) and DEM particles. The particle colors are chosen randomly.

Plotting the packing density for all granules in figure 5 over the relative effective cohesion ω_i/ω_o shows that this trend is generally observed for all dry cohesions. For the lowest dry cohesion of $\omega_o = 50 \text{ kN/m}^2$ we observe an asymptotic limit in the packing density at very low relative cohesions ($0 \leq \omega_i/\omega_o \leq 0.1$). Apart from this, the packing density appears to have an approximately linear relationship with the relative cohesion. Figure 5 also shows a dependency of the packing density on the dry cohesion ω_o , which is plotted in different line styles and increases from top to bottom.

In order to systematically investigate the granule morphology, we extracted the size of the shell and core regions of the granules as described in section 2.6. As a result, figure 6 shows the internal structure of the granules by plotting the radial extent of the inner zone (green) and the outer shell area (blue) as a function of the relative effective cohesion ω_i/ω_o . Each sub-figure represents one fixed dry cohesion, i.e. one line from figure 5. We recognize from figure 6 that all granules have a dense region on the outside and that most of them also feature a porous zone in the core. Only for cases with small effective cohesions ($\omega_o = 50 \text{ kN/m}^2$ with $\omega_i/\omega_o = 0, 0.1$ and $\omega_o = 150 \text{ kN/m}^2$ with $\omega_i/\omega_o = 0$) we observe completely dense granules. These three cases correspond to the topmost data points in the top left of figure 5.

3.2. Capillary force

The second goal of this study was to identify the influence of the capillary force on the formation of spray dried granules. As a baseline for this, the simulations with $\omega_o = 150 \text{ kN/m}^2$

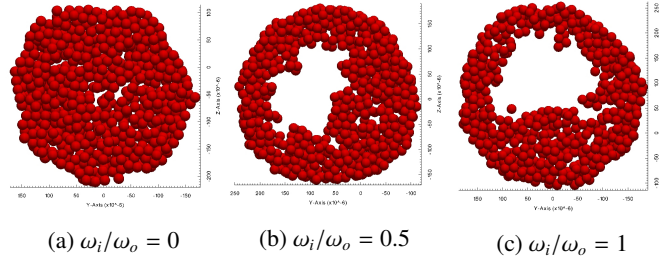


Figure 4: Cross sectional slices of selected spray dried granules ($\omega_o = 150 \text{ kN/m}^2$, $\sigma = \sigma_0$) with a thickness of roughly two DEM particles.

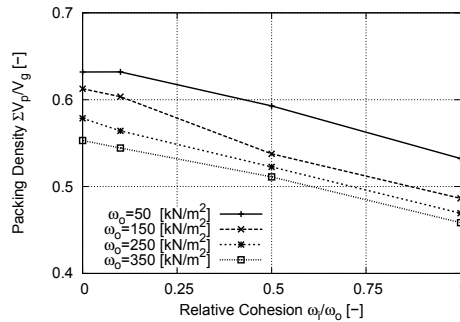


Figure 5: Mean packing density of dried granules for various ω_o as a function of the relative effective cohesion ω_i/ω_o .

were chosen, as these contain a representative spectrum of the results of section 3.1 ranging from a fully dense granule at an effective cohesion ratio of $\omega_i/\omega_o = 0$ to a thin shell for $\omega_i/\omega_o = 1$. On this basis, the capillary surface tension was varied in the next step within $\sigma = \{1/10, 1/3, 3, 10\} \cdot \sigma_0$, where $\sigma_0 = 7.07 \text{ mN/m}$ corresponds to section 3.1. The resulting granules were evaluated in terms of packing density. High packing densities correspond to dense granules whereas low densities correspond to hollow granules.

Figure 7 shows the packing density of the resulting granules as a function of the capillary surface tension for the different effective wet cohesions. We observe a strong dependency of the granule density on the capillary surface tension relating low surface tensions with low densities

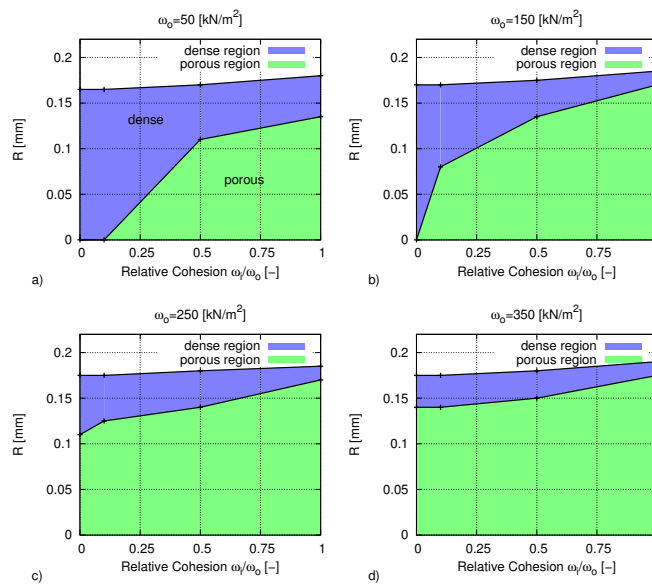


Figure 6: Dense (blue) and porous regions (green) inside spray dried granules for various effective dry cohesions ω_o as a function of the relative effective cohesion ω_i/ω_o .

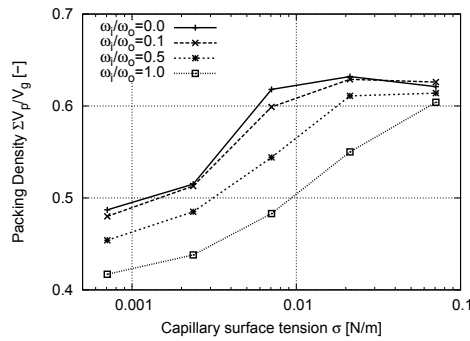


Figure 7: Mean packing density of dried granules for various ω_i/ω_o as a function of the capillary surface tensions σ .

and high surface tensions with high densities. The correlation is not linear, however. Indeed the mode of correlation itself depends on the effective cohesion as we observe a relatively smooth transition for high wet cohesions opposed to a rather sharp, almost step-like transition for low wet cohesion. In addition to this non-linear correlation, we find that the variance of the granule densities for different effective cohesions also depends on the capillary surface tension. At the base parameter $\sigma = \sigma_0$ we observe a relatively large variation of 13.5%. A low surface tension of $\sigma = 0.1\sigma_0$ results in 7% variance while a high surface tension of $\sigma = 10\sigma_0$ reduces the variance to 2.2%.

As previously done for the cases of varying effective cohesion, the granules with varying capillary surface tension were examined regarding their morphology. The results of this analysis are displayed in figure 8, where again the radial extent of the inner zone (green) and the outer shell area (blue) are plotted, however, in this case as a function of the capillary surface tension. Comparing figures 7 and 8, it can be seen that – as before – regions of low overall density correspond to granule morphologies with both a shell and a porous core of varying size. However, considering the shell dimensions, their thickness dropped going from high to low surface tensions (i.e. right to left) but only to a certain minimum value, which seems to exist for a given relative effective cohesion. In this region of minimum shell thickness, changes of surface tension do lead to a change of granule density, as seen in figure 7, but this change is related to a growth of the porous zone rather than shell thinning as seen at varying effective cohesions (figure 5).

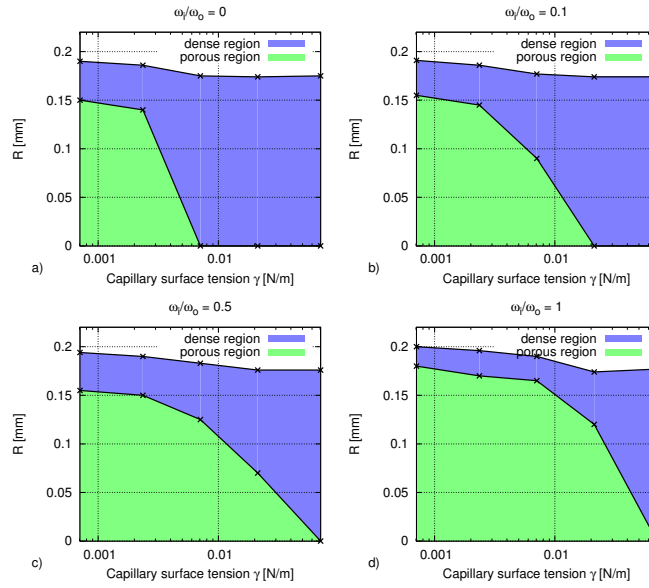


Figure 8: Same as figure 6, but for varying capillary surface tensions σ .

4. Discussion

4.1. Model interpretation – Strength of granular structures

The results in section 3.1 showed a clear correlation between bulk cohesive forces and granule density, relating dense granules with both low effective wet and dry cohesion and, on the other hand, low density granules with both high effective wet and dry cohesion. One reason for a change in the bulk cohesion (i.e. the strength of a network) of both dispersed and agglomerated primary particles could be the addition of binder to the suspension, as often seen in the processing of ceramics [3]. Hence, interpreting higher effective cohesion as a result of a rising binder content, our results agree well with both experimental and simulation data in literature [18, 37].

However, as the model we used does not specify precisely the physical nature of the bulk cohesion, interpreting the simulation results must be done with caution. As described in section 2.4, the effective cohesion in the proposed model does *not* directly correspond to the real intermolecular forces on the primary particle level. In a dispersed suspension, the intermolecular forces feature a repulsive barrier followed by an attractive van-der-Waals region on the short range, while, on the other hand, in an agglomerated suspension the primary particles are always attractive [3]. However, as the DEM particles in this work do not directly represent the individual primary particles but are always describing many of these, it is clear that the effective cohesion parameters must reflect not the intermolecular forces but the characteristics of many particles interacting. Therefore, it is important to note that, as illustrated in figure 2, an *agglomerated* suspension corresponds to *low cohesion* values whereas a *dispersed* suspension is reflected by a *high cohesion*. Under this premise, the simulation results of section 3.1 agree well with the qualitative finding that agglomerated suspensions form dense granules, while dispersed suspensions lead to hollow granules [4–9]. Figure 9 demonstrates this correlation by using experimental results of [6] and [7].

The reason for the relation described above is discussed in the following: The main mechanism of stabilization is the formation of a repulsive barrier while the attractive inter-particle forces do not change drastically when going from dispersed to agglomerated suspensions. Hence, the net attractive force per primary particle is smaller in an assembly of agglomerates as compared to an array of closely packed formerly dispersed particles once their repulsive barriers have been overcome. Assuming in a simplified thought experiment that the maximum force and number of contacts may be the same in both cases, this can also be seen from the Kirkwood tensor [38, 39]

$$\mathbf{P} = \frac{1}{V} \sum \mathbf{F} \otimes \mathbf{r}, \quad (17)$$

which describes the stress in a granular system. Here, V denotes the reference volume inside which the attractive forces \mathbf{F} occur in distance \mathbf{r} from the origin. Under these circumstances and for a single primary particle or agglomerate of radius r , the volume is $V \propto r^3$ as the contact forces appear always on the boundary of the particle or agglomerate, respectively. Hence, the maximum stress that can be carried by the particle or agglomerate before breaking the contacts with its neighbors is

$$\mathbf{P} \propto 1/r^2. \quad (18)$$

This means that the maximum stress which a particle network can carry decreases with increasing *effective* size of the particles. In our DEM simulations, however, the coarsened effective DEM particles represent many primary particles and the DEM particle size does not correspond to the size of the actual agglomerates or primary particles. Therefore, the interaction force law must convey this information via the empirical effective cohesion parameter.

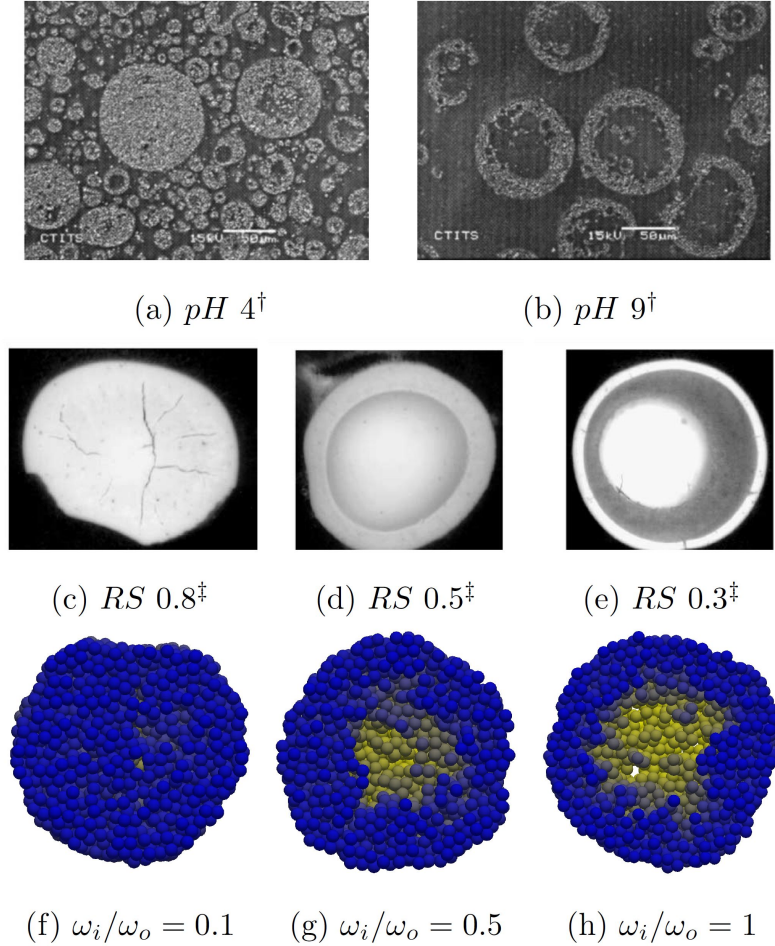


Figure 9: Experimentally manufactured granules (a-e) in comparison with simulation results (f-h). Granules (a) and (c) were made of agglomerated suspensions, while for granules (b), (d) and (e) dispersed suspensions were used. The simulations (f-h) have a growing relative effective cohesion ω_i/ω_o . ([†] from [6] and [‡] from [7], each with permission by Elsevier.)

4.2. Mechanisms of granule formation – A balance of forces

In the majority of the reports about investigations of the influence of suspension parameters on the granule morphology at spray drying, the influence of surface tension has not been studied in any detail – neither experimentally [2, 4, 5, 8, 9, 40] nor by means of numerical simulations [10–15, 17, 18]. This lack of information makes it hard to carry out immediate validation of the results by independent reference data. However, the results from section 3.2 are very promising and give at least a good qualitative insight. In the following, the effects we observed will be discussed in the context of capillary and cohesive forces.

As evaporation takes place, the solid particles are pushed towards the center of the drop by

the receding liquid surface, which corresponds to a concentration of particles beneath the drop surface. As the drying goes on, the evolution of the granule is dominated by two effects: (i) the formation of a more or less stable shell, whose physical strength is dominated by the effective bulk cohesion, and (ii) the compressive stress exerted on this network of particles by the capillary surface tension. Hence, if the compression is strong enough against the cohesive network, some bonds may break yielding ductile deformation and rearrangement of the particles, which leads to solid granules. In turn, if the strength of the cohesive bonds is strong against the capillary stress, the particle network may withstand the external load and the surface penetrates the shell, leading to a hollow granule.

In order to test this hypothesis, in figure 10 all granules from sections 3.1 and 3.2 have been revisited and their packing densities have been plotted as a function of the dimensionless number

$$\frac{\omega_i l}{\sigma} \iff \frac{\text{effective wet cohesion}}{\text{surface tension}}, \quad (19)$$

which describes the ratio of the effective wet cohesion force and the capillary force. The characteristic length scale l was chosen to be the granule diameter. The effective dry cohesion, which is not reflected in $\omega_i l/\sigma$, has been used as a color code for the data.

Figure 10 clearly indicates a strong correlation between the ratio of cohesive and capillary forces. A best fit of the function $f = a \log(\omega_i l/\sigma) + b$ with fit parameters a and b has been added in figure 10 as a dashed line to guide the eye. A linear regression in logarithmic space yields a level of confidence of $R^2 = 0.91$, which clearly indicates a significant correlation.

In this context it is remarkable that the effective dry cohesion ω_o seems to have only a minor influence on the structure formation of the granules as can be seen from the diffuse spreading of the colors indicating the dry cohesion in figure 10. This finding also fits well in the previously described model, as the main mechanisms that determine the evolution of the granule (i.e. compressive stress vs. network strength) happen inside the liquid phase. In combination with the

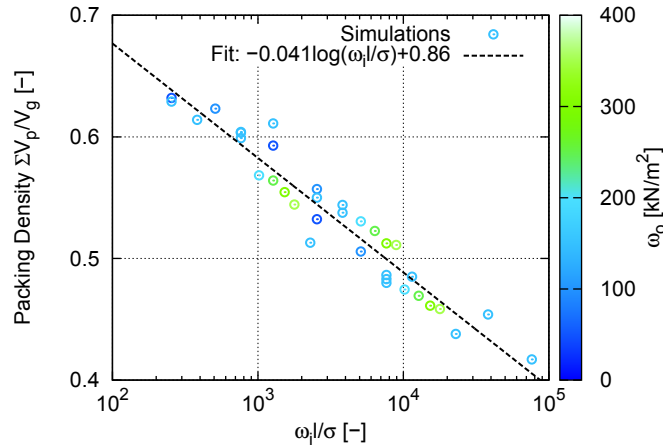


Figure 10: Overall packing density of the spray dried granules as a function of the dimensionless number $\omega_i l/\sigma$ as a measure for the ratio of cohesive and capillary forces.

interpolation between ω_i and ω_o near the surface (eq. 15) this results in the effective dry cohesion being only a supporting factor after the liquid surface passed but not the main component dominating the granule strength during formation. Simplifying the previous statement, it can be summarized as: The effective dry cohesion only starts to fully act once the main competition between effective wet cohesion and capillary forces is already settled.

5. Summary and Conclusions

A coupled CFD-DEM solver was used to study the influence of cohesive and capillary forces on the evolution of the granule morphologies of spray dried ceramics and a clear, significant correlation was found between these forces and the granule packing density and morphology. This relates dense granules with low cohesive forces (corresponding to agglomerates) and high capillary forces (and vice versa). Furthermore, a logarithmic relationship was found between the ratio of the wet cohesive and capillary force and the granule density with a high level of confidence.

As a result of the detailed view gained by particle simulations of the drying process, an explanation of the results was provided that extends the established concept of particle mobility [4, 6, 7] by the influence of shell strength and stability: The formation of hollow granules cannot be satisfactorily explained by particle mobility alone because the evolving shell needs some internal strength in order to resist the compression by the receding liquid surface. It has been shown that the strength of the shell in comparison to the compressive capillary stress must be taken into account as well to describe the behavior observed in experiments.

6. Acknowledgment

This research has been partially supported by the EU FP7 Project SimPhoNy (grant number 604005) and the German Research Foundation (DFG) under grant WO 1667/1-1.

References

- [1] S. Lukasiewicz, Spray-drying ceramic powders, *Journal of the American Ceramic Society* 72 (4) (1989) 617–624.
- [2] S. Lukasiewicz, J. Reed, Character and compaction response of spray-dried agglomerates, *American Ceramic Society Bulletin* 57 (1978) 798–801.
- [3] J. A. Lewis, Colloidal processing of ceramics, *Journal of the American Ceramic Society* 83 (10) (2000) 2341–2359.
- [4] W. J. Walker Jr., J. S. Reed, S. K. Verma, Influence of slurry parameters on the characteristics of spray-dried granules, *Journal of the American Ceramic Society* 82 (7) (1999) 1711–1719.
- [5] J. Tsubaki, H. Yamakawa, T. Mori, H. Mori, Optimization of granules and slurries for press forming, *Journal of the Ceramic Society of Japan* 110 (2002) 894–898.
- [6] G. Bertrand, C. Filiatre, H. Mahdjoub, A. Foissy, C. Coddet, Influence of slurry characteristics on the morphology of spray-dried alumina powders, *Journal of the European Ceramic Society* 23 (2) (2003) 263 – 271.
- [7] H. Mahdjoub, P. Roy, C. Filiatre, G. Bertrand, C. Coddet, The effect of the slurry formulation upon the morphology of spray-dried yttria stabilised zirconia particles, *Journal of the European Ceramic Society* 23 (10) (2003) 1637 – 1648.
- [8] F. L. G.E. Fair, Effect of interparticle potential on forming solid, spherical agglomerates during drying, *Journal of the American Ceramic Society* 87 (2004) 4–9.
- [9] G. Bertrand, P. Roy, C. Filiatre, C. Coddet, Spray-dried ceramic powders: A quantitative correlation between slurry characteristics and shapes of the granules, *Chemical Engineering Science* 60 (1) (2005) 95 – 102.
- [10] A. Lee, C. Law, Gasification and shell characteristics in slurry droplet burning, *Combustion and Flame* 85 (1-2) (1991) 77–93.
- [11] M. Kadja, G. Bergeles, Modelling of slurry droplet drying, *Applied Thermal Engineering* 23 (7) (2003) 829–844.

- [12] H. Liang, K. Shinohara, H. Minoshima, K. Matsushima, Analysis of constant rate period of spray drying of slurry, *Chemical Engineering Science* 56 (6) (2001) 2205–2213.
- [13] C. S. Handscomb, M. Kraft, A. E. Bayly, A new model for the drying of droplets containing suspended solids, *Chemical Engineering Science* 64 (4) (2009) 628–637.
- [14] C. S. Handscomb, M. Kraft, A. E. Bayly, A new model for the drying of droplets containing suspended solids after shell formation, *Chemical Engineering Science* 64 (2) (2009) 228–246.
- [15] C. S. Handscomb, M. Kraft, Simulating the structural evolution of droplets following shell formation, *Chemical Engineering Science* 65 (2) (2010) 713–725.
- [16] P. Greil, J. Cordelair, A. Bezold, Discrete element simulation of ceramic powder processing, *Zeitschrift Fur Metallkunde* 92 (7) (2001) 682–689.
- [17] D. Nishiura, A. Shimosaka, Y. Shirakawa, J. Hidaka, Simulation of drying of particulate suspensions in spray-drying granulation process, *Journal of Chemical Engineering of Japan* 43 (8) (2010) 641–649.
- [18] S. Miyazaki, D. Nishiura, A. Shimosaka, Y. Shirakawa, J. Hidaka, Revealing the formation mechanism of granules by drying simulation of slurry droplet, *Advanced Powder Technology* 22 (1, SI) (2011) 93–101.
- [19] OpenFOAM Foundation, OpenFOAM@documentation, www.openfoam.org (2014).
- [20] J. U. Brackbill, D. B. Kothe, C. Zemach, A continuum method for modeling surface tension, *Journal of Computational Physics* 100 (2) (1992) 335–354.
- [21] T. B. Anderson, R. Jackson, A fluid mechanical description of fluidized beds, *Industrial & Engineering Chemistry Fundamentals*.
- [22] P. Cundall, O. Strack, A discrete numerical model for granular assemblies, *Geotechnique* 29 (1) (1979) 47–65.
- [23] S. Luding, About contact force-laws for cohesive frictional materials in 2d and 3d, in: *Behavior of Granular Media*, 2006.
- [24] C. Thornton, S. J. Cummins, P. W. Cleary, An investigation of the comparative behaviour of alternative contact force models during elastic collisions, *Powder Technology* 210 (3) (2011) 189–197.
- [25] H. Hertz, ber die berhrung fester elastischer krper, *Journal fr die reine und angewandte Mathematik* 92 (1881) 156–171.
- [26] E. D. Landau, E. M. Lifshitz, *Theory of Elasticity*, Pergamon Press, 1970.
- [27] J. U. Brackbill, D. B. Kothe, *Dynamical modeling of surface tension*, Tech. rep., Los Alamos National Lab., NM (United States) (1996).
- [28] B. Lafuire, C. Nardone, R. Scardovelli, S. Zaleski, G. Zanetti, Modelling merging and fragmentation in multiphase flows with surfer, *Journal of Computational Physics* 113 (1994) 134–147.
- [29] D. J. E. Harvie, M. R. Davidson, M. Rudman, An analysis of parasitic current generation in volume of fluid simulations, *Australian and New Zealand Industrial and Applied Mathematics Journal* 46 (E) (2005) C133–C149.
- [30] T. Breinlinger, A. Hashibon, T. Kraft, Simulation of the influence of surface tension on granule morphology during spray drying using a simple capillary force model, Submitted to *Powder Technology*.
- [31] P. A. Kralchevsky, K. Nagayama, Capillary forces between colloidal particles, *Langmuir* 10 (1) (1994) 23–36.
- [32] P. K. Kundu, I. M. Cohen, *Fluid mechanics*, Academic Press (Elsevier), 2008, iSBN 978-0-12-373735-9.
- [33] P. Roy, G. Bertrand, C. Coddet, Spray drying and sintering of zirconia based hollow powders, *Powder Technology* 157 (1'3) (2005) 20 – 26.
- [34] R. Larson, *The structure and rheology of complex fluids*, Oxford University Press, 1998.
- [35] C. Bierwisch, T. Kraft, H. Riedel, M. Moseler, Three-dimensional discrete element models for the granular statics and dynamics of powders in cavity filling, *Journal of the Mechanics and Physics of Solids* 57 (1) (2009) 10–31.
- [36] SciPy developers, SciPy (2014).
URL <http://docs.scipy.org>
- [37] Y. Zhang, X. Tang, N. Uchida, K. Uematsu, Binder surface segregation during spray drying of ceramic slurry, *Journal of Materials Research* 13 (1998) 1881–1887.
- [38] R. G. Larson, *The structure and rheology of complex fluids*, Oxford University Press, 1999.
- [39] J. Bardet, I. Vardoulakis, The asymmetry of stress in granular media, *International Journal of Solids and Structures* 38 (2) (2001) 353 – 367.
- [40] J. Reeds, Spray drying and implications for compactibility of product granules, *Ceramic Engineering and Science Proceedings* 18 (1997) 343?358.